Electric field modulation of magnetism in ferrimagnetic Heusler heterostructures

Qilong Sun,[1,*] Sohee Kwon,[1] Maria Stamenova,[2] Stefano Sanvito,[2] and Nicholas Kioussis[1,†]
[1]*Department of Physics and Astronomy, California State University, Northridge, California 91330-8268, USA*
[2]*School of Physics, AMBER and CRANN Institute, Trinity College, Dublin 2, Ireland*

(Received 6 December 2019; revised manuscript received 4 March 2020; accepted 23 March 2020; published 15 April 2020)

To date the realization of magnetoresistive random access memory (RAM) and magnetoelectric RAM (MeRAM) devices relies primarily on ultrathin ferromagnetic-based (FeCoB/MgO) magnetic tunnel junctions. On the other hand, the Heusler family of intermetallics is considered very promising for spintronic applications. Nevertheless, the voltage controlled magnetic anisotropy (VCMA) in ultrathin Heusler-based magnetic-tunnel junction stacks remains unexplored. Here, using the ferrimagnetic Heusler Mn_3Ga as a prototype system, we report *ab initio* calculations of the electric field modulation of magnetism in the $Ir/Mn_3Ga/MgO$ heterostructure. The trilayer structures with one and three monolayer Ir caps and Mn-Mn termination exhibit large perpendicular magnetic anisotropy in contrast to those with Mn-Ga termination which yield in-plane magnetization orientation. We predict giant VCMA coefficients the magnitude and sign of which depend on both the interface termination and the Ir cap thickness. The underlying atomistic mechanism lies on the electric-field-induced shifts of the spin-orbit coupling energies of the spin-polarized Ir/d orbitals with different orbital angular momentum symmetries. Our paper paves the way for exploiting the unique magnetic properties of ferrimagnetic Heusler compounds for next generation MeRAM devices.

DOI: 10.1103/PhysRevB.101.134419

The engineering of perpendicular magnetic tunnel junctions (MTJs) has attracted enormous interest in the development of nonvolatile, high-performance, and low-power magnetoresistive random access memory (MRAM) devices using the spin-transfer-torque (STT) or spin-orbit-torque (SOT) writing schemes [1–5]. High magnetocrystalline anisotropy (MCA) for the MTJs is required to endow an easier operation scheme and higher stability for the recorded data against thermal fluctuations during reading [6]. On the other hand, large MCA entails higher power consumption during the writing process where the magnetization switching by spin-polarized currents inevitably leads to Joule heating [7]. Thus, one of the present challenges in implementing STT- or SOT-MRAM lies in the reduction of the intrinsic current density for magnetization switching while maintaining high thermal stability for long-term data retention [8].

The voltage-controlled magnetic anisotropy (VCMA) is a highly promising magnetization switching approach which may enable ultralow power, highly scalable, and nonvolatile magnetoelectric random access memory (MeRAM) [9,10]. The VCMA effect has been experimentally demonstrated in MgO-based MTJs, in the form of voltage-induced ferromagnetic resonance excitations [11], coherent precessional magnetization switching [12], dynamic magnetization switching [13,14], and spin-wave excitations [15]. Several different voltage-induced mechanisms have been proposed to elucidate the VCMA effect, including modification of the electronic structure at the interface [6,16–20], magnetic dipole moment [8], and the Rashba effect [21]. Two major challenges for future MeRAM devices are to achieve large perpendicular magnetic anisotropy (PMA) ($\geqslant 2$ erg/cm^2) and high VCMA efficiency, $\geqslant 1000$ fJ/V m, which will allow higher thermal stability, low-power (< 1 fJ/bit switching energy) and fast (< 1 ns) low-error write operations [22].

To date the realization of STT-MRAM and MeRAM devices relies primarily on ferromagnetic-based heterostructures, such as FeCoB/MgO MTJs [23,24]. Unfortunately, the PMA of ultrathin FeCo films arises from the interface between the FM layers and the tunnel barrier and/or the heavy metal (Ta, Hf, Ru) underlayer. The PMA in X/FeCo/MgO (X= Ta, Hf and Ru) heterostructures [7,25–27] is too weak (less than 2.3 erg/cm^2) to overcome thermal fluctuations when the device has a critical dimension less than about 20 nm [28]. In addition, experiments in FeCo/MgO-based MTJs have reported low VCMA efficiency values in the range from 100 to 300 fJ/V m depending on the capping material, such as Ta, Au, and Ir [29–31].

Thus, there is an urgent need in searching for and identifying magnetic materials in which the PMA and the VCMA efficiency is high. One of the most promising classes of materials are the Heusler compounds among which ($I4/mmm$ space group) Mn_3Ga is considered a prototype system with promising applications in the area of spintronics [32,33]. Its tetragonal $D0_{22}$ phase is a ferrimagnet exhibiting a unique combination of interesting properties, such as low saturation magnetization [34], high perpendicular uniaxial magnetic anisotropy [35], high-spin polarization [36–38], high Curie temperature [39], and low Gilbert damping constant [36]. In

*long.q.sun@gmail.com
†nick.kioussis@csun.edu

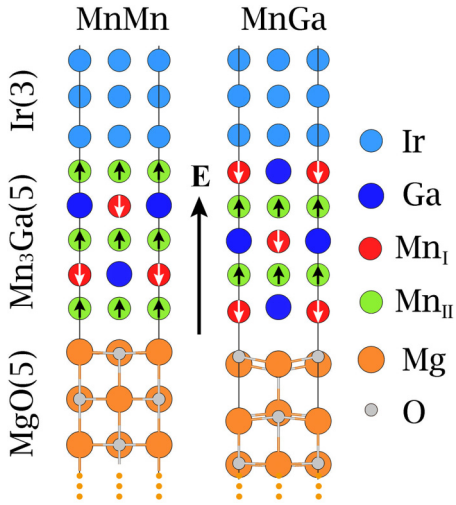

FIG. 1. Schematic atomic structures of the $Ir/Mn_3Ga/MgO$ layers with Mn_{II}-Mn_{II} (left) and Mn_I-Ga (right) terminations. The black arrow shows the direction of positive electric field and the z axis.

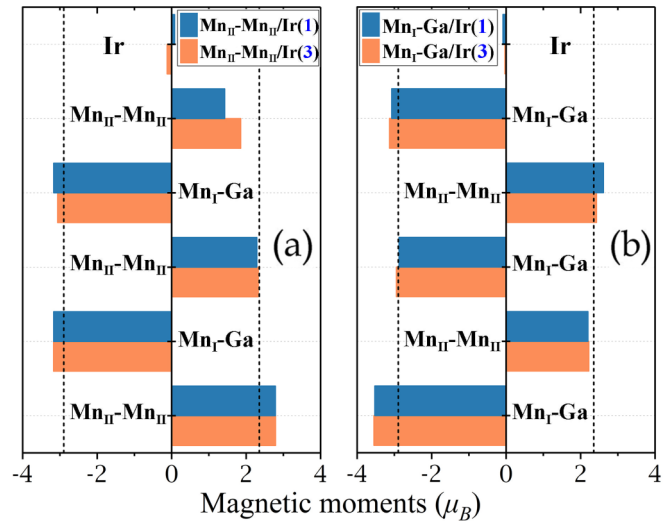

FIG. 2. Layer-resolved magnetic moments for the (a) Mn_{II}-Mn_{II}- and (b) Mn_I-Ga-terminated interfaces of the Ir(n ML)/Mn_3Ga(5 ML)/MgO(5 ML) heterostructure, for $n = 3$ (orange bars) and $n = 1$ (blue bars), respectively. The dashed vertical lines denote the corresponding layer-resolved bulk values.

contrast, the modulation of PMA and electric field control of magnetism in ferrimagnetic Heusler-based heterostructures remains unexplored thus far.

In this paper we investigate the effect of the electronic and magnetic properties of the $Ir/Mn_3Ga/MgO$ trilayer structures with different Mn_3Ga terminations (as shown in Fig. 1) based on first-principles calculations. The thin Ir overlayer was considered because it was shown to increase both the PMA and VCMA efficiency in FeCo-based heterostructures [40–44].

Density functional theory (DFT) calculations within the projector augmented-wave (PAW) method [45] were carried out using the Vienna *ab initio* simulation package [46]. We use the generalized gradient approximation to describe the exchange-correlation energy as parametrized by Perdew *et al.* [47]. In the $D0_{22}$ structure the two (001) antiferromagnetically coupled Mn sublattices consist of Mn_I atoms located at the Wyckoff positions $2b$ (0,0,1/2) [Mn_I-Ga plane] and Mn_{II} atoms at the $4d$ (0,1/2,1/4) positions [Mn_{II}-Mn_{II} plane]. The slab supercell for the Ir(n)/Mn_3Ga/MgO heterostructure, shown in Fig. 1, consists of $n = 1$ or 3 monolayers (MLs) of fcc Ir placed along [001] atop 5 MLs of Mn_3Ga and 5 MLs of rocksalt MgO underlayer. Here, the interfacial Mn and Ga atoms are placed atop the O atoms of the MgO surface, which are the most stable stacking configurations [48]. The in-plane lattice constant for the Ir(n)/Mn_3Ga/MgO heterostructures is set equal to the experimental value of 3.92 Å for the tetragonal Mn_3Ga system. This results in a compressive biaxial strain on the MgO of about −6.8% and a tensile biaxial strain of about +2.1% on the Ir cap [49]. A 15-Å vacuum space is adopted to separate the periodic films and the dipole corrections are taken along [001]. The plane-wave cutoff energy was set to 500 eV and a $16 \times 16 \times 1$ k mesh was used in the Brillouin-zone (BZ) sampling for the relaxation calculations. The atomic coordinates are fully optimized until the forces acting on the ions become less than 10^{-2} eV/Å, while those for the two bottommost MgO layers were kept frozen at their relaxed bulk positions. As shown in Fig. 1 we considered both the Mn_{II}-Mn_{II}- and Mn_I-Ga-terminated interfaces. For the MCA calculations, SOC was included with a $32 \times 32 \times 1$ k-point mesh. The MCA per unit interfacial area is determined from $E_{MCA} = (E_{[100]} - E_{[001]})/A$, where $E_{[100]}$ and $E_{[001]}$ represent the total energy with in-plane and out-of-plane magnetization, respectively, and A is the in-plane area of the unit cell.

Figure 2 shows the layer-resolved spin moments for the (a) Mn_{II}-Mn_{II}- and (b) Mn_I-Ga-terminated interfaces of the Ir(nML)/Mn_3Ga(5 ML)/MgO(5 ML) heterostructure, for $n = 3$ (orange bars) and $n = 1$ (blue bars), respectively. Our calculated values of the bulk magnetic moments of -2.90 μ_B and 2.35 μ_B for the Mn_I and Mn_{II} atoms, respectively, denoted by the dashed vertical lines are in good agreement with previous DFT calculations [33,49]. The magnetic moments of the Mn_I and Mn_{II} atoms in the central layer are about -3.1 and 2.3 μ_B, respectively. One can see that the magnetic moments of the interfacial Mn_I or Mn_{II} atoms next to the MgO for the Mn_I-Ga or Mn_{II}-Mn_{II} terminations are enhanced to -3.55 μ_B and 2.79 μ_B, respectively, compared to their bulk values due to the O/p-Mn/d hybridization. In contrast, the two neighboring Ga and O ions in the Mn_IGa/MgO interface tend to repulse each other without any overlapping of electron localization, leading to the rough interfaces as shown in Fig. 1. Notably, the average magnetic moments of the interfacial Mn_{II} atoms next to the Ir cap are dramatically reduced to the values of 1.86 and 1.42 μ_B for the 3 ML and 1 ML Ir cap, respectively. The underlying mechanism for such moment reduction is the change of the spin-polarized projected density of states (DOS), shown in Fig. 3(a), on the interfacial Mn_{II} next to Ir compared to those of the central Mn_{II}. More specifically, there is a decrease of the occupied majority-spin Mn_{II}-derived DOS compared to those of the central Mn_{II} layer due to the significant hybridization of the Mn_{II}-derived d_{yz} and d_{z^2} states with the corresponding interfacial Ir/d-derived states. In contrast, there is small change of the minority-spin Mn_{II}-derived states (primarily of d_{xy} character). These two

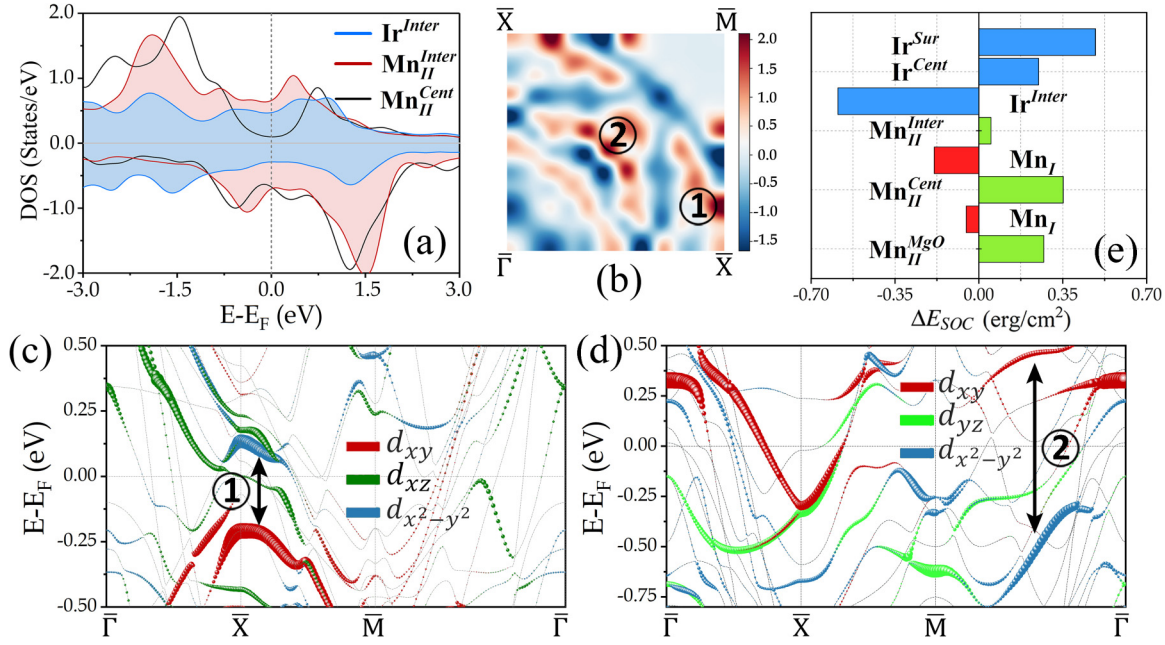

FIG. 3. (a) Atom-resolved spin-polarized DOS for the interfacial Mn_{II}, central Mn_{II}, and interfacial Ir atoms of the Mn_{II}-Mn_{II}-terminated interface of the Ir(3)/Mn_3Ga(5)/MgO(5) heterostructure. (b) **k**-resolved MCA, MCA(**k**) (in erg/cm^2) in the two-dimensional BZ. Energy- and **k**-resolved distributions of the d-orbital character of (c) minority-spin and (d) majority-spin bands along the symmetry directions for the interfacial Mn_{II} atom. Numerals in panels (b)–(d) refer to BZ **k** points where the MCA is large. (e) Average layer-resolved SOC energy differences, ΔE_{SOC}, per Mn or Ir atom.

effects lead to the significant reduction of the Mn_{II} moment. The magnetic moment of ∼0.1 μ_B of the interfacial Ir atom for the Ir(1)/Mn_3Ga/MgO trilayer is much smaller than that of 0.7 μ_B in the Ir(1 ML)/FeCo/MgO, indicating a stronger hybridization effect in the Ir/Mn_3Ga interface [42,43]. On the other hand, the emergence of magnetism on the Ir atoms in the Ir(3)/Mn_3Ga(5)/MgO(5) heterostructures can be attributed to the proximity effect as the freestanding 3 ML Ir is nonmagnetic.

Table I lists values of the MCA (calculated from total energies) for the (a) Mn_I-Ga- and (b) Mn_{II}- Mn_{II}-terminated interfaces of the Ir(n ML)/Mn_3Ga(5 ML)/MgO(5 ML) heterostructure for different Ir-cap thickness. The calculations reveal that the Mn_I-Ga-terminated interface overall favors an in-plane magnetization orientation for $n \leqslant 3$, while the Mn_{II}-Mn_{II}-terminated interface yields an out-of-plane orientation. Furthermore, the latter heterostructure with a single Ir cap yields a colossal PMA of 24.75 erg/cm^2 which can be attributed to the large SOC constant of the magnetic Ir overlayer, similar to that of the Ir(1 ML)/FeCo/MgO system [42]. In addition, we have also employed the force theorem where [19] MCA = $\sum_{\mathbf{k}}$ MA(**k**) to calculate the termination-dependent MCA. The k-resolved MCA(**k**) ≈ $\sum_{n\in occ}[\varepsilon(n,\mathbf{k})^{[100]} - \varepsilon(n,\mathbf{k})^{[001]}]$ in the two-dimensional (2D) BZ. Here, $\varepsilon(n,\mathbf{k})^{[100](([001])}$ are the eigenvalues of the Hamiltonian for magnetization along the [100] ([001]) direction. The MCA values calculated from the force theorem, also listed in brackets in Table I, agree well with those obtained from total-energy calculations. Also, it should be noted that the MCA decreases monotonically with increasing Ir cap thickness ($n = 5, 7$) for the Mn_{II}-Mn_{II} termination while it shows an opposite behavior for the Mn_I-Ga termination. Since thicker Ir caps ($n > 3$ ML) yield MCA values <2 erg/cm^2, throughout the remaining paper we focus only on the configurations for $n \leqslant 3$.

TABLE I. Values of the MCA (in erg/cm^2), calculated from differences in total energy, for the (a) Mn_I-Ga- and (b) Mn_{II}-Mn_{II}-terminated interfaces of the Ir(n ML)/Mn_3Ga(5 ML)/MgO(5 ML) heterostructure, for different Ir-cap thickness. The MCA values in brackets are calculated using the force theorem.

Ir thickness (ML)	Mn_I-Ga termination	Mn_{II}-Mn_{II} termination
1	−1.78 (−1.70)	24.75 (24.75)
3	−0.14 (−0.14)	2.65 (2.61)
5	−0.09 (−0.09)	−0.97 (−0.96)
7	1.16 (1.17)	−1.77 (−1.78)

The calculated k-resolved MA(**k**) for the Mn_{II}-Mn_{II}-terminated interface for the 3 ML Ir cap is shown in Fig. 3(b). The origin of the hot k spots, 1 and 2, can be understood from the second-order perturbation theory MCA expression, given by [44]

$$\text{MCA} \approx \sum_{I,lmm'\sigma\sigma'} \sum_{o,u} \sigma\sigma' \xi_{Il}^2 \frac{P_u^{Ilm\sigma} P_o^{Ilm'\sigma'}}{E_u^{\sigma} - E_o^{\sigma'}} \Delta L_{l,mm'}, \quad (1)$$

where

$$\Delta L_{l,mm'} = |\langle lm|\hat{L}_z|lm'\rangle|^2 - |\langle lm|\hat{L}_x|lm'\rangle|^2. \quad (2)$$

Here, $\sigma, \sigma' \equiv \pm 1$ denote the electron spin; $\hat{\xi}$ is a diagonal matrix containing the SOC strength; $\hat{L}_{x(z)}$ is the $x(z)$ component of the orbital angular momentum operator; and $P_n^{Ilm\sigma} = |\langle \Psi_n^{\sigma}||Ilm\rangle|^2$ is the Bloch wave amplitude projected

on atom I, orbital index lm, and spin index σ, where $\Psi_n^\sigma(E_n^\sigma)$ are the one-electron occupied and unoccupied spin-polarized Bloch states (energies) of band index n and wave vector k (omitted for simplicity). Analysis of the orbital-resolved band structures of the interfacial Mn and Ir atoms shows that only the Mn_{II} atoms are primarily responsible for the hot spots 1 and 2 in the k-resolved MCA in Fig. 3(b), which yield the dominant contribution to the interfacial MCA. In Figs. 3(c) and 3(d) we show the energy- and k-resolved distribution of the minority- and majority-spin bands, respectively, of the interfacial Mn_{II}-derived d_{xy}, d_{xz}, and $d_{x^2-y^2}$ states along the high-symmetry directions of the 2D BZ. The maximum of MCA($k_\parallel$) at point 1 (around $\frac{1}{4}\overline{\mathrm{XM}}$) in Fig. 3(b) arises from the SOC between the minority-spin interfacial Mn_{II}-derived occupied d_{xy} states with the unoccupied $d_{x^2-y^2}$ states through the out-of-plane $\hat{L}_z$ operator. The large positive MCA at point 2 (around $\frac{1}{2}\overline{\Gamma\mathrm{M}}$) in Fig. 3(b) arises from the SOC of $\langle d_{xy}|\hat{L}_z|d_{x^2-y^2}\rangle$ of the majority-spin states of interfacial Mn_{II}. In contrast, the negative MCA around $\frac{1}{2}\overline{\Gamma\mathrm{X}}$ is mainly derived from the SOC between minority-spin (majority-spin) occupied d_{xy} (d_{yz}) and unoccupied d_{xz} (d_{xy}) through the in-plane orbital angular momentum, $\hat{L}_x$. The vanishing MCA($k_\parallel$) around $\overline{\mathrm{M}}$ in Fig. 3(b) is due to the absence of interfacial Mn_{II}-derived states near the Fermi level.

We have also calculated the atom-resolved SOC energy difference, $\Delta E_{\mathrm{SOC}} = (E_{\mathrm{SOC}}^{\parallel} - E_{\mathrm{SOC}}^{\perp})/2$, for the Mn_{II}-Mn_{II} terminated Ir(3 ML)/Mn_3Ga(5 ML)/MgO(5 ML) heterostructure. Here, $E_{\mathrm{SOC}}^{\parallel}$ and $E_{\mathrm{SOC}}^{\perp}$ are the SOC energies with in-plane ($\parallel$) and out-of-plane ($\perp$) magnetization orientation, given by

$$E_{\mathrm{soc}} = \frac{\hbar^2}{2m^2c^2}\left\langle \frac{1}{r}\frac{dV}{dr}\hat{L}\cdot\hat{S}\right\rangle, \tag{3}$$

where $V(r)$ is the spherical part of the effective potential within the PAW sphere. Figure 3(e) shows the average layer-resolved ΔE_{SOC} per Mn or Ir atom. Note that the MCA $\neq \Delta E_{\mathrm{SOC}}$ is due to the failure of perturbation theory for the Ir atoms which have large SOC constant ($\approx$0.45 eV) [44]. However, one can see that the average ΔE_{SOC} of 0.35 erg/cm^2 per Mn atom for the central Mn_{II}-Mn_{II} layer is close to the corresponding bulk value of $\approx$0.41 erg/cm^2. This suggests that the ΔE_{SOC} energies of the bottom three Mn_3Ga layers away from the Ir cap do follow the perturbative treatment in SOC. Since the MCA of the bottom three Mn_3Ga layers is about 1.2 erg/cm^2, the corrected ΔE_{SOC} for the interfacial Mn_3Ga/Ir layers would be about 1.45 erg/cm^2, yielding a total MCA of 2.65 erg/cm^2. These results demonstrate that both interface contributions to the MCA are equally important for thin Mn_3Ga films.

Figure 4 shows the variation of the MCA as a function of the electric field in MgO for the (a) Mn_I-Ga- and (b) Mn_{II}- Mn_{II} terminated interfaces of the Ir(nML)/Mn_3Ga(5 ML)/MgO(5 ML) heterostructure for both the 1 ML and 3 ML Ir cap, respectively. In the linear regime, VCMA $= \Delta$(MCA) $= E_{\mathrm{MCA}}(E_{\mathrm{ext}}) - E_{\mathrm{MCA}}(0) = \beta E_{\mathrm{I}} = \beta E_{\mathrm{ext}}/\epsilon_\perp$, where β is the VCMA efficiency, E_{I} is the electric field inside the insulator, and $\epsilon_\perp$ is the out-of-plane component of the relative dielectric constant tensor of the insulator which depends on strain and the type of the insulator [19,20]. The results reveal that both the interface termination

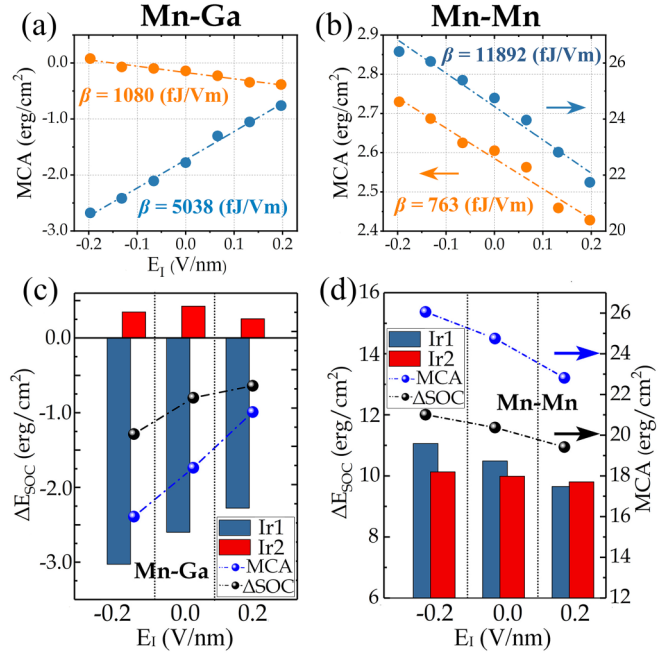

FIG. 4. Magnetic anisotropy as a function of electric field in MgO for the (a) Mn_I-Ga and (b) Mn_{II}-Mn_{II} terminations for the Ir(n)/Mn_3Ga/MgO heterostructure with $n = 1$ ML (blue circles) and $n = 3$ ML (orange circles), respectively. Difference in total SOC energies between the in- ($\parallel$) and out-of-plane ($\perp$) magnetization orientation, ΔE_{SOC} (blue circles), and MCA energies (black circles) for the (c) Mn_I-Ga and (d) Mn_{II}-Mn_{II} terminations of the Ir(n)/Mn_3Ga/MgO heterostructure with $n = 1$ ML, under zero and $\pm$0.19 V/nm electric field in the insulator. Bar graphs represent the atom-resolved ΔE_{SOC} for the two nonequivalent interfacial Ir atoms.

and the thickness of the iridium cap have a dramatic effect on the magnitude and sign of the VCMA efficiency. For the Mn_I-Ga termination β changes from +5038 fJ/V m to −1080 fJ/V m for the 1 ML and 3 ML Ir cap, respectively, while for the Mn_{II}-Mn_{II} termination β changes from −118 92 fJ/V m to −763 fJ/V m for the 1 ML and 3 ML Ir cap, respectively. These VCMA values are about a factor of 3–20 higher compared to the range of about 20–300 fJ/(V m) of most experimentally reported values for the FeCo-based MTJs [31,50]. In addition, we find that the VCMA efficiency of the heterostructure with 5 ML Ir cap reduces further to 446 (916) fJ/V m for the $Mn_{II}-Mn_{II}$ (Mn_I-Ga) termination.

In order to understand the microscopic origin of the giant VCMA efficiency of the 1 ML Ir cap, we show in Fig. 4 the electric field variation of the difference in SOC energy for the (c) Mn_I-Ga- and (d) $Mn_{II}-Mn_{II}$- terminated interfaces, respectively, for the Ir(1 ML)/Mn_3Ga(5 ML)/MgO(5 ML) system. For comparison, we also show the electric field dependence of the MCA calculated from difference of total energies (blue circles). One can see that $\Delta E_{\mathrm{SOC}} \propto$ MCA and $d\Delta E_{\mathrm{SOC}}/dE_{\mathrm{I}} \simeq d\mathrm{MCA}/dE_{\mathrm{I}} = \beta$. We also display the atom-resolved ΔE_{SOC} of the two interfacial Ir atoms (Ir_1 and Ir_2) on the same layer. The different contributions of interfacial Ir_1 and Ir_2 to the ΔE_{SOC} arise from their asymmetric nature when the magnetization is in plane. For both types of interface terminations the Ir_1-resolved ΔE_{SOC} yields the

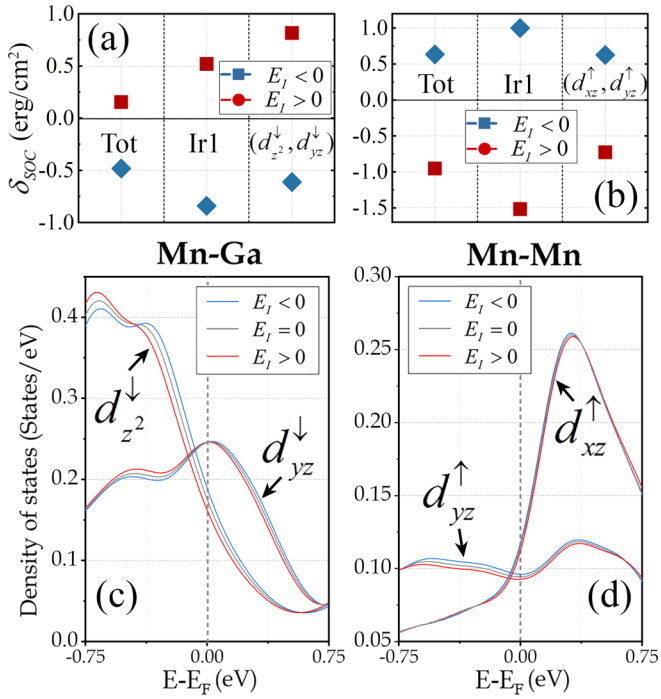

FIG. 5. E-field-induced change of SOC energies, $\delta_{\rm SOC} = \Delta E_{\rm SOC}(\mathbf{E}_{\rm I}) - \Delta E_{\rm SOC}(\mathbf{E}_{\rm I} = 0)$, for (a) $\rm Mn_I$-Ga and (b) $\rm Mn_{II}-Mn_{II}$ terminations, respectively. We also show the dominant Ir-d-orbital-projected $\langle d^{\downarrow}_{z^2}|\hat{L}_x|d^{\downarrow}_{yz}\rangle$ and $\langle d^{\uparrow}_{xz}|\hat{L}_z|d^{\uparrow}_{yz}\rangle$ contributions to $\delta E_{\rm SOC}$ for the two terminations, respectively. The spin-projected DOS of d_{z^2}, d_{xz}, and d_{yz} orbitals for Ir in the heterostructures with the (c) $\rm Mn_I$-Ga and (d) $\rm Mn_{II}-Mn_{II}$ terminations. The $E_{\rm I} > 0$ ($E_{\rm I} < 0$) denotes the applied E field of $+0.19$ (-0.19) V/nm in the insulator.

dominant contribution to the total $\Delta E_{\rm SOC}$, due to the larger SOC of the Ir atom ($\xi \sim 451$ meV) compared to that of Mn ($\xi \sim 42$ meV). Furthermore, we find a sign reversal of the VCMA efficiency from the $\rm Mn_I$-Ga to the $\rm Mn_{II}-Mn_{II}$ termination. In order to understand its origin we have calculated the Ir-5d orbital-projected contributions to $\Delta E_{\rm SOC}$. In Fig. 5 we show the *E-field-induced change* of $\Delta E_{\rm SOC}$, $\delta_{\rm SOC} = \Delta E_{\rm SOC}(\mathbf{E}_{\rm I}) - \Delta E_{\rm SOC}(\mathbf{E}_{\rm I} = 0)$, under $+0.19$ V/nm (red circles) and -0.19 V/nm (blue circles) for the (a) $\rm Mn_I$-Ga- and (b) $\rm Mn_{II}-Mn_{II}$-terminated interfaces, respectively, of the Ir(1 ML)/$\rm Mn_3Ga$(5 ML)/MgO(5 ML) heterostructure. For the $\rm Mn_I$-Ga termination we find that the E-field-induced change of SOC energies arises from the SOC of the $d^{\downarrow}_{z^2}$- and $d^{\downarrow}_{yz}$-derived states of interfacial $\rm Ir_1$ [as shown in Fig. 5(a)] via the in-plane orbital angular momentum operator, $\hat{L}_x$. The $\langle d^{\downarrow}_{z^2}|\hat{L}_x|d^{\downarrow}_{yz}\rangle$ in turn increases (decreases) under positive (negative) electric field. In sharp contrast, the $\rm Mn_{II}-Mn_{II}$ termination renders the $\langle d^{\uparrow}_{xz}|\hat{L}_z|d^{\uparrow}_{yz}\rangle$ dominant which in turn decreases (increases) under negative (positive) E field.

In addition the electric field has a significant effect primarily on the $d^{\downarrow}_{z^2}$- and $d^{\downarrow}_{yz}$-derived $\rm Ir_1$ projected density of states, shown in Figs. 5(c) and 5(d) for the $\rm Mn_I$-Ga and $\rm Mn_{II}-Mn_{II}$ terminations, respectively, of the Ir(1 ML)/$\rm Mn_3Ga$(5 ML)/MgO(5 ML) heterostructure. For the $\rm Mn_I$-Ga termination the Ir-$d^{\downarrow}_{z^2}$- and Ir-$d^{\downarrow}_{yz}$-derived DOS shift downward in energy with increasing electric field, leading to the reduction of the number of occupied d_{z^2} and unoccupied d_{yz} states near the Fermi level. Consequently, the dominant contribution of the in-plane orbital angular momentum, $\langle d^{\downarrow}_{z^2}|\hat{L}_x|d^{\downarrow}_{yz}\rangle$, in Eq. (2) decreases, leading to an increase of the MCA. In contrast, for the $\rm Mn_{II}-Mn_{II}$ termination the Ir-$d^{\uparrow}_{xz}$ occupied DOS shift downward in energy with increasing electric field, leading to a decrease of the out-of-plane orbital angular momentum matrix element, $\langle d^{\uparrow}_{xz}|\hat{L}_z|d^{\uparrow}_{yz}\rangle$, and hence a negative VCMA coefficient.

In summary, *ab initio* electronic structure calculations have been employed to investigate the electric field modulation of magnetism of ultrathin heterostructures based on the ferrimagnetic $\rm Mn_3Ga$ compound. The Ir cap induces large PMA for the $\rm Mn_{II}$-$\rm Mn_{II}$ interface termination which, however, changes to in-plane magnetization orientation for the $\rm Mn_I$-Ga-terminated interface. In addition to the termination type, the number of Ir layers also shows significant effect on the MCA values of the trilayer structures, leading to the spin reorientation. We predict record-high VCMA coefficients exceeding the required 1000 fJ/(V m) threshold, the magnitude and sign of which depend dramatically on the interface layer termination and Ir cap thickness. We have elucidated that the atomistic mechanism is the electric-field-induced shifts of SOC energies of the Ir/d orbitals with different orbital angular momentum symmetries. We hope that these predictions will rekindle experimental interest in the search for Heusler ferrimagnets for the next generation of nonvolatile and ultralow-power MeRAM devices.

We would like to thank Farzad Mahfouzi for useful discussions. The work is supported by NSF ERC-Translational Applications of Nanoscale Multiferroic Systems (TANMS) Grant No. 1160504. Q.S. was partially supported by the US Army under Grant No. W911NF-15-1-0066. S.K. was supported by NSF Partnership in Research and Education in Materials Grant No. DMR-1828019.

[1] J. C. Slonczewski, Current-driven excitation of magnetic multilayers, J. Magn. Magn. Mater. **159**, L1 (1996).

[2] L. Berger, Emission of spin waves by a magnetic multilayer traversed by a current, Phys. Rev. B **54**, 9353 (1996).

[3] A. D. Kent, Perpendicular all the way, Nat. Mater. **9**, 699 (2010).

[4] M. Wang, W. Cai, D. Zhu, Z. Wang, J. Kan, Z. Zhao, K. Cao, Z. Wang, Y. Zhang, T. Zhang, C. Park, J.-P. Wang, A. Fert, and W. Zhao, Field-free switching of a perpendicular magnetic tunnel junction through the interplay of spin-orbit and spin-transfer torques, Nat. Electron. **1**, 582 (2018).

[5] F. Mahfouzi and N. Kioussis, First-principles study of the angular dependence of the spin-orbit torque in Pt/Co and Pd/Co bilayers, Phys. Rev. B **97**, 224426 (2018).

[6] J. Zhang, P. V. Lukashev, S. S. Jaswal, and E. Y. Tsymbal, Model of orbital populations for voltage-controlled magnetic anisotropy in transition-metal thin films, Phys. Rev. B **96**, 014435 (2017).

[7] F. Matsukura, Y. Tokura, and H. Ohno, Control of magnetism by electric fields, Nat. Nanotechnol. **10**, 209 (2015).

[8] S. Miwa, M. Suzuki, M. Tsujikawa, K. Matsuda, T. Nozaki, K. Tanaka, T. Tsukahara, K. Nawaoka, M. Goto, Y. Kotani, T. Ohkubo, F. Bonell, E. Tamura, K. Hono, T. Nakamura, M. Shirai, S. Yuasa, and Y. Suzuki, Voltage controlled interfacial magnetism through platinum orbits, Nat. Commun. **8**, 15848 (2017).

[9] M. Weisheit, S. Fähler, A. Marty, Y. Souche, C. Poinsignon, and D. Givord, Electric field-induced modification of magnetism in thin-film ferromagnets, Science **315**, 349 (2007).

[10] T. Maruyama, Y. Shiota, T. Nozaki, K. Ohta, N. Toda, M. Mizuguchi, A. Tulapurkar, T. Shinjo, M. Shiraishi, S. Mizukami, Y. Ando, and Y. Suzuki, Large voltage-induced magnetic anisotropy change in a few atomic layers of iron, Nat. Nanotechnol. **4**, 158 (2009).

[11] T. Nozaki, Y. Shiota, S. Miwa, S. Murakami, F. Bonell, S. Ishibashi, H. Kubota, K. Yakushiji, T. Saruya, A. Fukushima, S. Yuasa, T. Shinjo, and Y. Suzuki, Electric-field-induced ferromagnetic resonance excitation in an ultrathin ferromagnetic metal layer, Nat. Phys. **8**, 491 (2012).

[12] Y. Shiota, T. Nozaki, F. Bonell, S. Murakami, T. Shinjo, and Y. Suzuki, Induction of coherent magnetization switching in a few atomic layers of FeCo using voltage pulses, Nat. Mater. **11**, 39 (2012).

[13] C. Grezes, F. Ebrahimi, J. G. Alzate, X. Cai, J. A. Katine, J. Langer, B. Ocker, P. K. Amiri, and K. L. Wang, Ultra-low switching energy and scaling in electric-field-controlled nanoscale magnetic tunnel junctions with high resistance-area product, Appl. Phys. Lett. **108**, 012403 (2016).

[14] S. Kanai, M. Yamanouchi, S. Ikeda, Y. Nakatani, F. Matsukura, and H. Ohno, Electric field-induced magnetization reversal in a perpendicular-anisotropy CoFeB-MgO magnetic tunnel junction, Appl. Phys. Lett. **101**, 122403 (2012).

[15] Y. J. Chen, H. K. Lee, R. Verba, J. A. Katine, I. Barsukov, V. Tiberkevich, J. Q. Xiao, A. N. Slavin, and I. N. Krivorotov, Parametric resonance of magnetization excited by electric field, Nano Lett. **17**, 572 (2017).

[16] C.-G. Duan, J. P. Velev, R. F. Sabirianov, Z. Zhu, J. Chu, S. S. Jaswal, and E. Y. Tsymbal, Surface Magnetoelectric Effect in Ferromagnetic Metal Films, Phys. Rev. Lett. **101**, 137201 (2008).

[17] K. Nakamura, R. Shimabukuro, Y. Fujiwara, T. Akiyama, T. Ito, and A. J. Freeman, Giant Modification of the Magnetocrystalline Anisotropy in Transition-Metal Monolayers by An External Electric Field, Phys. Rev. Lett. **102**, 187201 (2009).

[18] M. K. Niranjan, C.-G. Duan, S. S. Jaswal, and E. Y. Tsymbal, Electric field effect on magnetization at the Fe/MgO(001) interface, Appl. Phys. Lett. **96**, 222504 (2010).

[19] P. V. Ong, N. Kioussis, D. Odkhuu, P. K. Amiri, K. L. Wang, and G. P. Carman, Giant voltage modulation of magnetic anisotropy in strained heavy metal/magnet/insulator heterostructures, Phys. Rev. B **92**, 020407 (2015).

[20] P. V. Ong, N. Kioussis, P. K. Amiri and K. L. Wang, Electric-field-driven magnetization switching and nonlinear magnetoelasticity in Au/FeCo/MgO heterostructures, Sci. Rep. **6**, 29815 (2016).

[21] S. E. Barnes, J. Ieda, and S. Maekawa, Rashba spin-orbit anisotropy and the electric field control of magnetism, Sci. Rep. **4**, 4105 (2014).

[22] X. Li, A. Lee, S. A. Razavi, H. Wu, and K. L. Wang, Voltage-controlled magnetoelectric memory and logic devices, MRS Bull. **43**, 970 (2018).

[23] S. Ikeda, K. Miura, H. Yamamoto, K. Mizunuma, H. D. Gan, M. Endo, S. Kanai, J. Hayakawa, F. Matsukura, and H. Ohno, A perpendicular-anisotropy CoFeB–MgO magnetic tunnel junction, Nat. Mater. **9**, 721 (2010).

[24] S. S. P. Parkin, C. Kaiser, A. Panchula, P. M. Rice, B. Hughes, M. Samant, and S.-H. Yang, Giant tunnelling magnetoresistance at room temperature with MgO (100) tunnel barriers, Nat. Mater. **3**, 862 (2004).

[25] T. Liu, J. W. Cai, and L. Sun, Large enhanced perpendicular magnetic anisotropy in CoFeB/MgO system with the typical Ta buffer replaced by an Hf layer, AIP Adv. **2**, 032151 (2012).

[26] C. Pai, M. Nguyen, C. Belvin, L. H. Vilela-Leao, D. C. Ralph and R. A. Buhrman, Enhancement of perpendicular magnetic anisotropy and transmission of spin-Hall-effect-induced spin currents by a Hf spacer layer in W/Hf/CoFeB/MgO layer structures, Appl. Phys. Lett. **104**, 082407 (2014).

[27] D. C. Worledge, G. Hu, D. W. Abraham, J. Z. Sun, P. L. Trouilloud, J. Nowak, S. Brown, M. C. Gaidis, E. J. O'Sullivan and R. P. Robertazzi, Spin torque switching of perpendicular Ta|CoFeB|MgO -based magnetic tunnel junctions, Appl. Phys. Lett. **98**, 022501 (2011).

[28] S. V. Faleev, Y. Ferrante, J. Jeong, M. G. Samant, B. Jones, and S. S. P. Parkin, Heusler compounds with perpendicular magnetic anisotropy and large tunneling magnetoresistance, Phys. Rev. Mater. **1**, 024402 (2017).

[29] T. Nozaki, Y. Shiota, M. Shiraishi, T. Shinjo, and Y. Suzuki, Voltage-induced perpendicular magnetic anisotropy change in magnetic tunnel junctions, Appl. Phys. Lett. **96**, 022506 (2010).

[30] M. Endo, S. Kanai, S. Ikeda, F. Matsukura, and H. Ohno, Electric-field effects on thickness dependent magnetic anisotropy of sputtered $MgO/Co_{40}Fe_{40}B_{20}/Ta$ structures, Appl. Phys. Lett. **96**, 212503 (2010).

[31] Y. Kato, H. Yoda, Y. Saito, S. Oikawa, K. Fujii, M. Yoshiki, K. Koi, H. Sugiyama, M. Ishikawa, T. Inokuchi, N. Shimomura, M. Shimizu, S. Shirotori, B. Altansargai, Y. Ohsawa, K. Ikegami, A. Tiwari and A. Kurobe, Giant voltage-controlled magnetic anisotropy effect in a crystallographically strained CoFe system, Appl. Phys. Express **11**, 053007 (2018).

[32] B. S. Yang, L. N. Jiang, W. Z. Chen, P. Tang, J. Zhang, X.-G. Zhang, Y. Yan, and X. F. Han, First-principles study of perpendicular magnetic anisotropy in ferrimagnetic $D0_{22}-Mn_3X$ (X = Ga, Ge) on MgO and $SrTiO_3$, Appl. Phys. Lett. **112**, 142403 (2018).

[33] B. Balke, G. H. Fecher, J. Winterlik, and C. Felser, Mn_3Ga, a compensated ferrimagnet with high Curie temperature and low magnetic moment for spin torque transfer applications, Appl. Phys. Lett. **90**, 152504 (2007).

[34] F. Wu, S. Mizukami, D. Watanabe, H. Naganuma, M. Oogane, Y. Ando, and T. Miyazaki, Epitaxial $Mn_{2.5}Ga$ thin films with giant perpendicular magnetic anisotropy for spintronic devices, Appl. Phys. Lett. **94**, 122503 (2009).

[35] Z. Bai, Y. Cai, L. Shen, M. Yang, V. Ko, G. Han, and Y. Feng, Magnetic and transport properties of $Mn_{3-x}Ga/MgO/Mn_{3-x}Ga$ magnetic tunnel junctions: A first-principles study, Appl. Phys. Lett. **100**, 022408 (2012).

[36] S. Mizukami, F. Wu, A. Sakuma, J. Walowski, D. Watanabe, T. Kubota, X. Zhang, H. Naganuma, M. Oogane, Y. Ando, and T. Miyazaki, Long-Lived Ultrafast Spin Precession in Manganese Alloys Films with a Large Perpendicular Magnetic Anisotropy, Phys. Rev. Lett. **106**, 117201 (2011).

[37] H. Kurt, K. Rode, M. Venkatesan, P. Stamenov, and J. M. D. Coey, High spin polarization in epitaxial films of ferrimagnetic Mn_3Ga, Phys. Rev. B **83**, 020405(R) (2011).

[38] J. Winterlik, B. Balke, G. H. Fecher, C. Felser, M. C. M. Alves, F. Bernardi, and J. Morais, Structural, electronic, and magnetic properties of tetragonal $Mn_{3-x}Ga$ Experiments and first-principles calculations, Phys. Rev. B **77**, 054406 (2008).

[39] E. Kren and G. Kadar, Neutron diffraction study of Mn_3Ga, Solid State Commun. **8**, 1653 (1970).

[40] T. Nozaki, A. Koziol-Rachwal, M. Tsujikawa, Y. Shiota, X. Xu, T. Ohkubo, T. Tsukahara, S. Miwa, M. Suzuki, S. Tamaru, H. Kubota, A. Fukushima, K. Hono, M. Shirai, Y. Suzuki, and S. Yuasa, Highly efficient voltage control of spin and enhanced interfacial perpendicular magnetic anisotropy in iridium-doped Fe/MgO magnetic tunnel junctions, NPG Asia Mater. **9**, e451 (2017).

[41] K. Nakamura, T. Nomura, A. M. Pradipto, K. Nawa, T. Akiyama, and T. Ito, Effect of heavy-metal insertions at Fe/MgO interfaces on electric-field-induced modification of magnetocrystalline anisotropy, J. Magn. Magn. Mater. **429**, 214 (2017).

[42] S. Kwon, P. V. Ong, Q. Sun, F. Mahfouzi, X. Li, K. L. Wang, Y. Kato, H. Yoda, P. K. Amiri, and N. Kioussis, Colossal electric field control of magnetic anisotropy at ferromagnetic interfaces induced by iridium overlayer, Phys. Rev. B **99**, 064434 (2019).

[43] D. Odkhuu, S. H. Rhim, N. Park, and S. C. Hong, Extremely large perpendicular magnetic anisotropy of an Fe(001) surface capped by 5d transition metal monolayers: A density functional study, Phys. Rev. B **88**, 184405 (2013).

[44] S. Kwon, Q. Sun, F. Mahfouzi, K. L. Wang, P. K. Amiri, and N. Kioussis, Voltage-Controlled Magnetic Anisotropy in Heterostructures with Atomically Thin Heavy Metals, Phys. Rev. Appl. **12**, 044075 (2019).

[45] P. E. Blöchl, Projector augmented-wave method, Phys. Rev. B **50**, 17953 (1994).

[46] G. Kresse and J. Furthmüller, Efficient iterative schemes for ab initio total-energy calculations using a plane-wave basis set, Phys. Rev. B **54**, 11169 (1996).

[47] J. P. Perdew, K. Burke, and M. Ernzerhof, Generalized Gradient Approximation Made Simple, Phys. Rev. Lett. **77**, 3865 (1996).

[48] Y. Miura and M. Shirai, Theoretical study on tunneling magnetoresistance of magnetic tunnel junctions with $D0_{22}$-Mn_3Z (Z = Ga, Ge), IEEE Trans. Magn. **50**, 1 (2014).

[49] K. Rode, N. Baadji, D. Betto, Y.-C. Lau, H. Kurt, M. Venkatesan, P. Stamenov, S. Sanvito, J. M. D. Coey, E. Fonda, E. Otero, F. Choueikani, and P. Ohresser, F. Porcher, and G. André, Site-specific order and magnetism in tetragonal Mn_3Ga thin films, Phys. Rev. B **87**, 184429 (2013).

[50] X. Li, K. Fitzell, D. Wu, C. T. Karaba, A. Buditama, G. Yu, K. L. Wong, N. Altieri, C. Grezes, N. Kioussis, S. Tolbert, Z. Zhang, J. P. Chang, P. Khalili Amiri, and K. L. Wang, Enhancement in the interfacial perpendicular magnetic anisotropy and the voltage-controlled magnetic anisotropy by heavy metal doping at the Fe/MgO interface, Appl. Phys. Lett. **110**, 052401 (2017).